THE ASTROPHYSICAL JOURNAL, 310:552–560, 1986 November 15

COMPTONIZATION IN SUPERCRITICAL WINDS. II. DYNAMICS AND OBSERVATIONAL DIAGNOSTICS

PETER A. BECKER[1] AND MITCHELL C. BEGELMAN[1,2]
Joint Institute for Laboratory Astrophysics, University of Colorado and National Bureau of Standards
Received 1985 December 16; accepted 1986 May 2

ABSTRACT

We investigate the dynamics of radiatively driven, optically thick outflow in this second of two papers addressing the observable properties of supercritical winds. When the sonic radius of the flow is well within the trapping radius, a simple relation links the mass-loss rate, the position of the sonic point, and the observed luminosity (which is always in excess of the Eddington limit). The variation of the wind velocity deep within the flow is determined by numerically solving the relativistic, adiabatic version of Bernoulli's equation, and the result is incorporated into the radiative transfer formalism of the first paper to calculate the radiative properties of supercritical winds for a variety of astrophysical systems.

Subject headings: galaxies: nuclei — hydrodynamics — quasars — radiation mechanisms — stars: winds — X-rays: bursts

I. INTRODUCTION

Optically thick winds driven by continuum radiation pressure have long been suspected of playing a role in systems ranging from X-ray binaries to active galactic nuclei (AGNs) (e.g., Meier 1982*a*, *b*, *c*). Recently, data have accumulated indicating that X-ray transients radiating above their Eddington limits L_E (Lewin and Joss 1981; McCray 1981) and quasars with outflow rates $\dot{M} > \dot{M}_E \equiv L_E/c^2$ (Drew and Boksenberg 1984; Krolik *et al.* 1985; Perry and Dyson 1985) may exist in nature. The purpose of this paper is to reevaluate the dynamics and appearance of supercritical winds (i.e., winds with $\dot{M} \gtrsim \dot{M}_E$) in the light of this evidence. We begin by summarizing some of the existing observational and theoretical work relevant to our investigation.

a) X-Ray Bursters

The observational evidence for super-Eddington luminosities in X-ray burst sources is twofold: (1) The maximum color temperature observed during a burst is typically ~ 2.5 keV, and sometimes as high as 3 keV (Swank, Taam, and White 1984), while general relativistic calculations show that a neutron star–size blackbody with temperature $T \gtrsim 2$ keV will radiate above its Eddington limit (Marshall 1982). (2) The observed integrated burst flux, when combined with an assumed mean source distance of ~ 9 kpc, often indicates that the burst luminosity is in excess of the Eddington limit for a 1.4 $M_\odot$ object.

By modeling the burst spectra as emission from gray (scattering-dominated) atmospheres, various authors have attempted to circumvent the first of these points by decoupling the observed color temperature of the burst from the effective temperature (defined by $\sigma T_{\rm eff}^4 = F_b$, where F_b is the bolometric burst flux at the source). Ebisuzaki, Hanawa, and Sugimoto (1984, EHS), for example, apply the standard photon diffusion equation (i.e., eq. [2.10]) to the photospheres of bright neutron stars to find that $T_{\rm color} \approx \tau_{\rm color}^{1/4} T_{\rm eff}$, where $\tau_{\rm color}$ is the scattering optical depth to the color radius (at which the observed color temperature equals the local electron temperature). A subsequent approximate analysis of the energy transfer due to inelastic scattering beyond the color photosphere ($r > r_{\rm color}$) leads EHS to conclude that $T_{\rm color}/T_{\rm eff} \approx 2^{1/2}$ at the peak of a typical burst. Assuming source radii of ~ 12 km, this would allow the bursts to be Eddington limited *if* the distance to the center of the burst source distribution (roughly the Galactic center) were moved from ~ 10 to ~ 6–7 kpc. In later works, Ebisuzaki and Nomoto (1985) and London, Taam, and Howard (1986) endeavor to provide accurate numerical treatments of the influence of Compton scattering on X-ray burst spectra. Their results (which again show $T_{\rm color} > T_{\rm eff}$), an extension of those published by London, Taam, and Howard (1984), are illustrated by Ebisuzaki and Nomoto using a color temperature-luminosity diagram which agrees fairly well with the observed temporal behavior of one burst from the source MXB 1636−536 (Inoue *et al.* 1984).

The controversy surrounding the nature of the X-ray burst sources hence pivots on the question of source distance, since most investigators agree that the bursts probably originate on the surfaces of unmagnetized neutron stars (thus restricting the central mass to a rather narrow range). If, as seems likely at present, the distance to the Galactic center is ~ 9 kpc, then the X-ray transients have peak luminosities exceeding $L_{\rm E}$ by factors as large as 10 (Lewin and Joss 1981), and total energies sufficient to propel perhaps 10^{19} g of matter out of the neutron star's potential well (McCray 1981).

b) Quasars and AGNs

Analysis of the broad absorption features apparent in the spectra of $\sim 5\%$ of all quasars with redshift $z > 1.5$ indicates that gas ejected from these systems may reach velocities of up to $0.1c$ (Weymann, Carswell, and Smith 1981). If the absorption occurs toward the outer, coasting (constant velocity) regions of a spherically symmetric, radiatively driven wind, then the mass-loss rate $\dot{M} = 4\pi r^2 \rho v$ is related to the column density N_i of the ionic species by

$$\frac{\dot{M}}{\dot{M}_{\rm E}} = \frac{2N_i u_\infty x_{\rm abs} \sigma_i}{g_i}, \qquad (1.1)$$

[1] Also at the Department of Astrophysical, Planetary, and Atmospheric Sciences, University of Colorado, Boulder, CO 80309.
[2] Presidential Young Investigator.

where u_∞ is the asymptotic flow speed divided by c, σ_i is the product of the Thomson cross section and the atomic weight, $x_{\rm abs} = r_{\rm abs}/r_{\rm S}$ is the distance from the continuum source to the absorption region in units of the Schwarzschild radius, and g_i is the ionic fraction by weight (suitably averaged over the line of sight if not constant).

While fairly reliable estimates for N_i have been obtained in some cases (Canizares and Kruper 1984; Turnshek 1984), the value of $x_{\rm abs}$ has remained elusive, since we do not even know if the absorption occurs near the quasar or far from it in the intergalactic medium (Weymann 1985, private communication). By studying the properties of the absorption region in the contexts of particular models, some progress has been made in bracketing the mass-loss rate for individual objects. Krolik *et al.* (1985) consider the ionization equilibrium of absorbing gas bathed in continuum radiation, taking into account resonant absorption of O VIII Lyα, to derive $\dot{M}$ for the BL Lac object PKS 2155−304. By comparing their numerical results with observations of a sharp absorption feature at 0.6 keV in the X-ray spectrum of the object, they find $\dot{M} \approx$ 300–1000 $M_\odot$ yr^{-1}. Drew and Boksenberg (1984) apply a moments method developed by Castor, Lutz, and Seaton (1981) to the optically thin Si IV λ1397 line profile of the broad absorption line (BAL) quasar Q1413+117 to estimate $\dot{M} \approx 40$ $M_\odot$ yr^{-1}, if the outflow is spherically symmetric. Perry and Dyson (1985) investigate shock formation as the generating and accelerating mechanism for clouds in the broad emission-line region (BLR) around a quasar or AGN. They also derive mass-loss rates which are high enough ($\dot{M} \approx$ 10–100 $M_\odot$ yr^{-1}) to push the outflow into the supercritical regime (see eq. [1.2] below). It is intriguing that the three treatments cited all yield sizable mass-loss estimates even though the studies focused on BL Lac objects, BAL quasars, and the BLRs of ordinary quasars, respectively.

c) *This Paper*

A spherically symmetric wind (or accretion flow) composed of fully ionized hydrogen is supercritical if

$$\dot{M} > \dot{M}_{\rm E} = (2.2 \times 10^{-9} M_\odot \text{ yr}^{-1}) \frac{M}{M_\odot}, \qquad (1.2)$$

where $\dot{M}_{\rm E} \equiv 4\pi G M m_{\rm H}/\sigma_{\rm T} c$ ($m_{\rm H}$ is the hydrogen mass, $\sigma_{\rm T}$ is the Thomson cross section, and M is the mass of the central object). For $M = 10^{9-11}$ $M_\odot$, the condition becomes $\dot{M} \gtrsim$ 2–200 $M_\odot$ yr^{-1}, which is consistent with the results for AGNs mentioned above. As we shall argue below, luminosities in excess of the Eddington limit in high-energy transients can also be understood in terms of supercritical winds.

The energy required to power the outflow in a supercritical wind might be provided by spherical supercritical accretion (Meier 1979), thermonuclear deflagrations or detonations in the outer layers of a neutron star (Hanawa and Sugimoto 1982; Taam 1982; Wallace, Woosley, and Weaver 1982; Paczyński 1983), or the rotational kinetic energy of a compact object spinning in a dense accretion cloud (the "cauldron" of Begelman and Rees 1983, 1984). As discussed in Becker and Begelman (1986, hereafter Paper I), the luminosity generated at the base of the flow is efficiently channeled into bulk acceleration of the gas when the scattering optical depth below the sonic (critical) radius r_c is so large that the flow velocity of the wind exceeds the diffusion velocity of the photons. For spherically symmetric winds this condition can be written as

$$r_c \ll r_t \equiv \frac{r_{\rm S}}{2} \frac{\dot{M}}{\dot{M}_{\rm E}}, \qquad (1.3)$$

where r_t is the trapping radius (at which the diffusion velocity of the photons equals the flow velocity) and $r_{\rm S} = 2GM/c^2$ is the Schwarzschild radius. Since the critical point must be outside the Schwarzschild radius to be physically meaningful, equation (1.3) is a somewhat more restrictive condition on $\dot{M}$ than is equation (1.2). We will henceforth use the term *supercritical* to refer to winds which satisfy the more restrictive condition, in keeping with Paper I. In this second of two papers dealing with the observable properties of supercritical winds, we discuss the dynamics of the relativistic flow of a radiation-dominated ideal fluid in the Schwarzschild metric, and incorporate the results into the radiative transfer formalism of Paper I to calculate the radiative properties for a variety of astrophysical systems.

Our discussion is organized as follows. In § II we combine Begelman's (1978) work on the dynamics of spherical flows in the Schwarzschild metric with the radiative transfer formalism for $r \gtrsim r_t$ developed in § V of Paper I to derive a relationship between the luminosity observed at infinity, the mass-loss rate, and the ratio $x_c \equiv r_c/r_{\rm S}$. In § III we consider the conditions in the region where the wind energy is injected into the flow (at $r = r_i$, the "injection radius"). Using energy conservation, we are able to solve for x_c and the wind velocity at the injection radius in terms of r_i and the initial specific enthalpy of the wind. In § IV we discuss the observable properties of supercritical winds for which the spectrum at r_i corresponds to optically thin bremsstrahlung emission. Finally, in § V we discuss the application of our theory to stellar-mass high-energy transients and to AGNs, and examine the accuracy of the various assumptions made here and in Paper I.

II. DYNAMICS

As discussed in Paper I, we assume for simplicity that all of the wind energy is deposited initially in a thin layer of matter near the base of the flow, probably through the action of some mechanical heating process (such as shocks or turbulence) which transports energy generated at a deeper level. We are interested in what happens when the integrated photon energy density (resulting from radiative cooling of the superheated matter in the injection region) becomes so large that the energy released through expansional cooling is sufficient to propel the gas through a sonic point and subsequently out of the gravitational potential well. In this section we apply Begelman's (1978) work on the relativistic hydrodynamics of matter-radiation flow to the case of a supercritical wind emanating from a compact object. The result is a relationship between the luminosity observed at infinity, the mass-loss rate, and the position of the transsonic point, which we subsequently untilize in § III to constrain the physical conditions in the injection region. Throughout the paper, we shall be dealing with spherically symmetric, radiation-dominated winds (in the Schwarzschild metric) composed of fully ionized hydrogen and characterized by the proper quantities electron temperature T_e, electron number density n_e ($= \rho/m_{\rm H}$), radiation pressure P_r, and radiation energy density U_r. We define $\tilde{u}$ as the magnitude of the spatial component of the wind's four-velocity, as measured by a stationary observer at infinity, i.e., $\tilde{u} \equiv (1/c)(dr/d\tau)$, where τ is the proper time. Finally, we associate the term *stationary* with reference frames that maintain a fixed position with

respect to the metric, while using the term *comoving* to refer to reference frames traveling outward with the local flow speed.

a) Relativistic, Radiation-dominated Winds

Our analysis begins with the equations governing the steady, spherically symmetric flow of a radiation-dominated ideal fluid in the Schwarzschild metric, as derived by Michel (1972):

$$Q\tilde{u}x^2 = \frac{c}{4\pi r_S^2}\dot{M}\,, \tag{2.1}$$

$$(1+4T)^2\left(1-\frac{1}{x}+\tilde{u}^2\right) = B_1\,, \tag{2.2}$$

where B_1 is constant, $Q \equiv \rho c^2$, $x \equiv r/r_S$, and we have defined the dimensionless temperature $T \equiv P_r/Q$ (note that T is distinct from T_e and that $r = xr_S$ is the radial coordinate measured by a stationary observer at infinity). If the relativistic region of the flow is well within the trapping radius, then the pressure of the photons decreases adiabatically according to

$$P_r \propto \rho^{4/3}\,, \tag{2.3}$$

and the dimensionless local sound speed, c_s, can be written as

$$c_s^2 = \frac{4T}{3(1+4T)} \tag{2.4}$$

(Weinberg 1972). Equations (2.1) and (2.2) can be combined to obtain a wind equation (Begelman 1978, eq. [3]) which satisfies the critical point conditions

$$\tilde{u}_c^2 = \frac{1}{4x_c}\,, \tag{2.5}$$

$$c_s^2(r_c) = \frac{4T_c}{3(1+4T_c)} = \frac{\tilde{u}_c^2}{1-3\tilde{u}_c^2} \tag{2.6}$$

(subscript c will be used to denote critical radius quantities throughout).

Note that the dimensionless flow velocity measured by a local observer who is stationary with respect to the metric,

$$u = \frac{\tilde{u}}{(1-1/x+\tilde{u}^2)^{1/2}}\,, \tag{2.7}$$

is equal to c_s at $r = r_c$; hence r_c is a sonic point in the usual sense. Using equations (2.3), (2.4), (2.5), and (2.6), we have

$$\frac{P_r}{\rho} = Tc^2 = \frac{3c^2}{16(x_c-3/2)}\left(\frac{\rho}{\rho_c}\right)^{1/3}\,, \tag{2.8}$$

which allows us to express the constant on the right side of Bernoulli's equation (2.2) as

$$B_1(x_c) = \frac{(x_c-3/4)^3}{x_c(x_c-3/2)^2}\,. \tag{2.9}$$

The diffusive luminosity L measured by an observer comoving with the flow is given by the photon diffusion equation

$$L = \frac{-4\pi r^2 c}{n_e\sigma_T}\frac{dP_r}{dr'}\,, \tag{2.10}$$

where dr' is measured in the comoving frame. For $x \gg 1$, general relativistic effects become unimportant, and we have in the adiabatic case

$$\frac{L}{L_E} = -\frac{4}{3}\gamma(u)\frac{r^2}{GM\rho}P_r\frac{d}{dr}\ln\rho\,, \tag{2.11a}$$

where $dr = \gamma(u)dr'$ denotes the radial increment measured by a stationary observer at infinity, and

$$\gamma(u) \equiv (1-u^2)^{-1/2} = (1+\tilde{u}^2)^{1/2} \tag{2.11b}$$

is the Lorentz factor. Combining equations (2.8) and (2.11a), the luminosity ratio can be expressed as

$$\frac{L}{L_E} = \gamma(u)\frac{x_c^{1/2}}{x_c-3/2}\left(\frac{x}{2\tilde{u}}\right)^{1/3}\left(1+\frac{1}{2}\frac{d\ln\tilde{u}}{d\ln x}\right), \tag{2.12}$$

where we have used equations (2.1) and (2.5) to write the density ratio in equation (2.8) as

$$\frac{\rho}{\rho_c} = \frac{x_c^{3/2}}{2\tilde{u}x^2}\,. \tag{2.13}$$

Using the critical point conditions (eqs. [2.5] and [2.6]), we can evaluate the luminosity at the critical radius:

$$\frac{L_c}{L_E} = \left(1+\frac{1}{4x_c}\right)^{1/2}\frac{x_c}{x_c-3/2}\left(1+\frac{1}{2}\frac{d\ln\tilde{u}}{d\ln x}\bigg|_{x_c}\right) \gtrsim 1\,. \tag{2.14}$$

The condition $L_c/L_E \gtrsim 1$ is what one would expect on physical grounds, since the gravitational and radiation forces on a particle should nearly balance at the critical point. Note that because the diffusive luminosity is an increasing function of x and $L_c/L_E \gtrsim 1$, the *asymptotic* diffusive luminosity is always in excess of the Eddington limit for the central mass.

For $x \gg x_c$, we expect the four-velocity $\tilde{u}$ to approach an asymptotic value $\tilde{u}_\infty$ if $T \to 0$ as $x \to \infty$. In this limit, equation (2.12) becomes

$$\frac{L}{L_E} = \gamma(u_\infty)\frac{x_c^{1/2}}{x_c-3/2}\left(\frac{x}{2\tilde{u}_\infty}\right)^{1/3}\,, \tag{2.15}$$

where the asymptotic four-velocity is defined by equations (2.2) and (2.9) as

$$\tilde{u}_\infty = \frac{\sqrt{3}}{2}\frac{[x_c^3-(3/4)x_c^2-(9/16)x_c]^{1/2}}{x_c(x_c-3/2)}\,. \tag{2.16}$$

Equation (2.16) indicates that as $x_c \to 3/2$, $\tilde{u}_\infty \to \infty$ (i.e., $u_\infty \to 1$), so that relativistic effects become important in the asymptotic portion of the wind. The analysis leading to equation (2.15) is valid provided $\tilde{u}$ effectively reaches $\tilde{u}_\infty$ within the trapping radius; otherwise, diffusion of photons becomes efficient enough to violate our assumption of an adiabatically decreasing photon energy density.

b) The Luminosity Observed at Infinity

For $\tilde{u} = \tilde{u}_\infty =$ constant, we can obtain an equation satisfied by U_r in the vicinity of and beyond the trapping radius (where adiabatic cooling and diffusion comprise the bulk of the relevant physics) by operating on Paper I, equation (5.1) with $\int_0^\infty v^3 dv$.[3] The result is

$$\frac{d^2U_r}{dr^2}+\left(\frac{4}{r}-\frac{3\tilde{r}_t}{r^2}\right)\frac{dU_r}{dr}-\frac{8\tilde{r}_t}{r^3}U_r = 0\,, \tag{2.17}$$

[3] The radial coordinate in Paper I, eq. (5.1) is measured in the comoving frame, and should therefore be replaced with r' to be consistent with the notation used in this paper. To obtain eq. (2.17), we have set the differential element of time measured in the comoving frame, $dt' = dr'/(u_\infty c)$, equal to the differential element of *proper* time measured by a stationary observer at infinity, $d\tau = dr/(\tilde{u}_\infty c)$, where $\tilde{u}_\infty = u_\infty\gamma(u_\infty)$.

where

$$\tilde{r}_t \equiv \frac{r_t}{\gamma^2(u_\infty)} . \tag{2.18}$$

Two factors of $\gamma(u_\infty)$ appear in equation (2.18) because the diffusion operator is second order in radius. Equation (2.17) is the $\alpha = 0$ case of Paper I, equation (B7), allowing us to immediately write down the solution in terms of Kummer's M function (Abramowitz and Stegun 1970, chap. 13),

$$U_r \propto q^3 M(\tfrac{1}{3}, 4, q) , \tag{2.19}$$

where

$$q \equiv -\frac{3\tilde{r}_t}{r} . \tag{2.20}$$

The diffusion approximation used in the derivation of equation (2.19) breaks down at large radii as free streaming becomes the dominant photon transport mechanism. We can estimate the maximum radius treatable under the diffusion approximation (the photospheric radius $r_p \equiv -3\tilde{r}_t/q_p$) by solving equation (5.11) of Paper I, which was derived by setting the diffusion velocity of the photons equal to the speed of light. With q_p determined, one can substitute equation (2.19) into equation (2.10) [with $U_r = 3P_r$ and $r^2/dr' = 3\tilde{r}_t\gamma(u_\infty)/dq$] to obtain another expression for L,

$$L = L_\infty \frac{M(1/3, 3, q)}{M(1/3, 3, q_p)} , \tag{2.21}$$

where L_∞ is the asymptotic diffusive luminosity and we have used equation (13.4.13) of Abramowitz and Stegun. As $r \to 0$ ($q \to -\infty$), equation (2.21) approaches

$$\frac{L}{L_\infty} = \frac{\Gamma(3)}{\Gamma(8/3)} \frac{(-q)^{-1/3}}{M(1/3, 3, q_p)} ; \tag{2.22}$$

using $q = (-3/2)(\dot{M}/\dot{M}_E)[\gamma^2(u_\infty)x]^{-1}$, we can eliminate L and x between equations (2.15) and (2.22) to obtain

$$\frac{L_\infty}{L_E} = 0.7171 \frac{x_c^{1/2}}{x_c - 3/2} \frac{(x_c - 3/4)^{1/2}}{[x_c^2 - (3/4)x_c - 9/16]^{1/6}} \times M\left(\frac{1}{3}, 3, q_p\right)\left(\frac{\dot{M}}{\dot{M}_E}\right)^{1/3} , \tag{2.23}$$

where we have also used equations (2.11b) and (2.16). We can estimate the quantity on the right-hand side of equation (2.23) to within 2% for $x_c \geq 2.5$ by setting $q_p = -3u_\infty$, which is the large r_p form of Paper I, equation (5.11). The quantity can be alternatively estimated to within 20% for $x_c \geq 2.5$ by setting $M(\frac{1}{3}, 3, q_p)$ equal to unity, which corresponds to the limit $r_p \to \infty$.

The qualitative features of this relationship can be recovered phenomenologically (Rees 1976, private communication; Meier 1982*a*) by coupling the photon diffusion equation (2.10) with the assumptions of pure adiabatic cooling below the trapping radius and pure diffusion beyond it, and the additional constraints $L_c \approx L_E$ and $u_c^{-2} \approx 4x_c$. One obtains the scaling law

$$\frac{L_\infty}{L_E} \approx (2x_c)^{-1/3}\left(\frac{\dot{M}}{\dot{M}_E}\right)^{1/3} \tag{2.24}$$

for constant velocity winds, which agrees quite closely with the relativistic result (eq. [2.23]) for $x_c \gg 1$. Both results indicate that the luminosity measured by a distant observer can be well in excess of L_E if the supercritical outflow passes through a sonic point located deep in the potential well; such super-Eddington luminosities are possible because the flow is optically thick and the radiation deep in the flow is trapped. Even though the diffusive luminosity surpasses the Eddington limit near the base of the flow and continues to grow thereafter, the rate of energy transport is not sufficient to wipe out the radiation pressure gradient over a dynamical time scale in such optically thick conditions. The diffusive luminosity builds until it reaches its asymptotic value (near the photosphere), as the flow becomes optically thin. In Figure 1, the upper, middle, and lower curves depict u_∞^{-1} (eqs. [2.7] and [2.16]), $\dot{m}^{1/3}l_\infty^{-1}$, and $\dot{m}^{1/3}l_{obs}^{-1}$, respectively, as functions of x_c, where $\dot{m} \equiv \dot{M}/\dot{M}_E$, $l_\infty \equiv L_\infty/L_E$ (eq. [2.23]), and $l_{obs} \equiv (1 + u_\infty)/(1 - u_\infty)l_\infty$. The l_{obs} curve corresponds to the luminosity measured by a distant observer *stationary* with respect to the central object, taking into account Doppler shifting. In the discussion following equation (2.14), we argue that l_∞ must always exceed unity, and therefore that $l_{obs} > (1 + u_\infty)/(1 - u_\infty)$. Combining this with the result for $\dot{m}^{1/3}l_\infty^{-1}$ contained in Figure 1, we find that radiation-dominated winds with $x_c \geq 2.5$ have mass-loss rates exceeding $\dot{M}_E$—a state of affairs which we shall see requires a prodigious energy generation rate in the injection region.

III. INJECTION RADIUS QUANTITIES

The injection radius r_i is defined as the radius within which all the energy in the wind is generated and injected into the flow. Beyond r_i, local energy conservation is satisfied and the photon energy density decreases nearly adiabatically (out to $r \approx r_t$) in the photon-dominated cases under consideration here.

a) Dynamical Considerations

The injection radius quantities T_i, ρ_i, x_i, and $\tilde{u}_i$ must satisfy equations (2.2), (2.8), and (2.13), where $B_1(x_c)$ is given by equa-

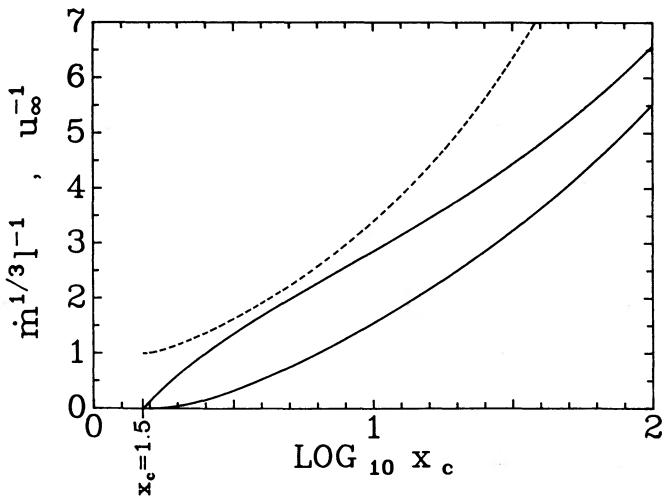

FIG. 1.—Upper (*dashed*) curve depicts the reciprocal of the asymptotic wind velocity $u_\infty^{-1} = \tilde{u}_\infty^{-1}(1 + \tilde{u}_\infty^2)^{1/2}$ as a function of x_c, calculated using eqs. (2.7) and (2.16). The lower two curves illustrate the dependence of $\dot{m}^{1/3}l^{-1}$ on x_c, where $\dot{m} \equiv \dot{M}/\dot{M}_E$. For the middle curve, $l = l_\infty \equiv L_\infty/L_E$ (eq. [2.23]) corresponds to the asymptotic luminosity measured in the comoving frame. For the lower curve, $l = l_{obs} = (1 + u_\infty)/(1 - u_\infty)l_\infty$ corresponds to the asymptotic luminosity measured by a stationary observer at infinity. According to the discussion following equation (2.14), l_∞ always exceeds unity, so that $l_{obs} > (1 + u_\infty)/(1 - u_\infty)$. Note that the importance of special relativity in the asymptotic portion of the wind increases as $x_c \to 3/2$.

tion (2.9). With T_i and x_i fixed, these equations can be solved simultaneously for x_c and $\tilde{u}_i$. For an established flow, it is interesting to ask what happens as x_i is gradually decreased, while holding T_i, $\tilde{u}_i$, and $\dot{M}$ constant. According to equations (2.2) and (2.9), x_c *increases*, since $dB_1/dx_c < 0$. To interpret this result physically, recall that the specific enthalpy of the wind is given by $c^2(P_r + U_r + Q)/Q = c^2(1 + 4T)$; hence the value of T_i sets the specific enthalpy of the fluid at the injection radius, or equivalently the amount of energy available to accelerate each gram of matter out of the potential well. As x_i decreases, more and more energy is required to propel a given $\dot{M}$ out to infinity, causing the terminal velocity of the wind to decrease. A decreased terminal velocity corresponds to a smaller velocity at the sonic surface, and hence an increased sonic radius.

If x_i were increased instead of decreased, eventually the injection and sonic radii would become coincident at what we define as $x_i = x_c = x_{\max}$. Using equation (2.8), we have

$$x_{\max} = \frac{3}{2}\left(1 + \frac{1}{8T_i}\right). \tag{3.1}$$

If x_i exceeds $x_{\max}$, the flow is already supersonic at the injection radius.

For any value of T_i, there is also a minimum value of x_i such that for $x_i < x_{\min}$, the flow never passes through a critical point. To estimate $x_{\min}$, note that for x_i near $x_{\min}$, $x_c \gg 1$ [so that $B_1(x_c) \approx 1$], which makes $\tilde{u}_c$ and $\tilde{u}_i$ negligibly small. Equation (2.2) then yields

$$x_{\min} = [1 - (1 + 4T_i)^{-2}]^{-1}. \tag{3.2}$$

Figure 2 illustrates the dependence of x_c on x_i for various values of T_i.

In the steady-state injection scenario we envisage, energy is pumped into the layer of superheated matter below r_i at a rate which is constant over many dynamical times. The superheated matter in turn maintains a fixed temperature by radiatively cooling until the photon pressure becomes large enough to drive a photospheric expansion. As radiation pressure propels the gas out of the injection region, the heating rate drops sharply and the specific enthalpy of the wind starts to decrease. The injection radius (by definition the radius at which the heating rate has essentially vanished) should therefore be about one radiation pressure scale height above the energy generation region (which should be near the "surface" of the compact object, at radius $r_0 \approx r_S$), i.e.,

$$x_i = x_0 + H, \tag{3.3}$$

where

$$H \equiv \frac{kT_{ei}}{\bar{m}g_0}\frac{P_{ri}}{P_{gi}}\frac{(1 - 1/x_0)^{1/2}}{r_S} = 2T_i x_0^2\left(1 - \frac{1}{x_0}\right) < x_0 \tag{3.4}$$

is the dimensionless radiation pressure scale height measured by an observer at infinity, $x_0 = r_0/r_S$, $\bar{m}$ is the average particle mass, $g_0 = GM(1 - x_0^{-1})^{-1/2}/r_0^2$ is the local gravitational acceleration (Weinberg 1972), and P_{ri} and P_{gi} are the photon and gas pressures at the injection radius, respectively. The accuracy of equation (3.4) is limited to $O(u_i)$, as the hydrostatic approximation implicit in the derivation breaks down for velocities approaching c.

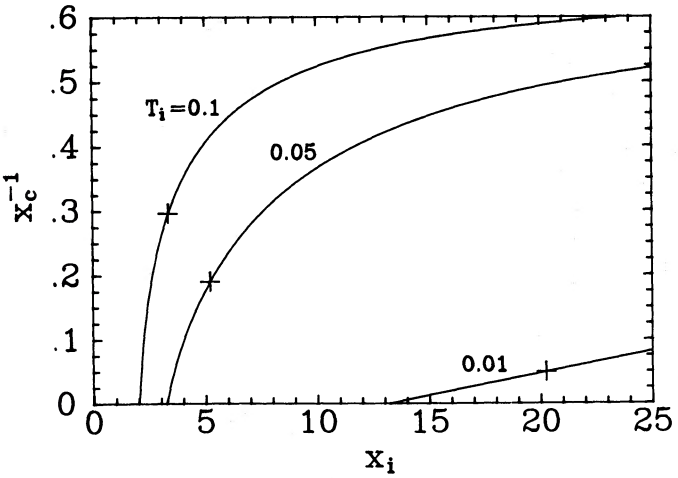

FIG. 2.—Reciprocal of x_c is plotted as a function of x_i, with the value of T_i indicated for each curve. The minimum value of x_i for each curve is the value that x_i must exceed for the outflow to pass through a critical point (eq. [3.2]; see the discussion in the text). The cross on each curve marks the point at which $x_i = x_c = x_{\max}$ (eq. [3.1]; if $x_i > x_{\max}$, $x_c < x_i$).

b) *Radiative Transfer*

In Paper I we develop a radiative transfer formalism which describes the effects of Compton scattering, adiabatic cooling, and diffusion on a photon distribution injected initially into the base of a supercritical wind. The spatial evolution within the "Comptonization region" (the region within which Compton scattering alters the spectrum) of the various physical quantities treated by the theory is expressed through their dependence on the frequency-independent Compton y-parameter (Paper I, eq. [2.10]), defined in the relativistic case as

$$y(r) = \int_{r_i}^{r} \frac{n_e \sigma_T kT_e}{m_e c^2}\frac{dr}{\tilde{u}}, \tag{3.5}$$

where m_e is the electron mass and r is measured by a stationary observer at infinity. We define the "Comptonization radius," r_β, as the radius at which y effectively reaches its asymptotic value, defined as β.

The spectral results for the Comptonization region are linked in Paper I, § V with solutions valid in a region which encompasses the trapping radius to predict the (comoving) spectrum observed at infinity. We show that for $r_\beta/r_t \ll 1$ (which corresponds to $r_\beta/\tilde{r}_t \ll 1$ in the relativistic case treated here), the exact value of r_β is irrelevant, since the Comptonization region is buried deep within the adiabatic (trapped) portion of the wind. In Paper I we assumed that the flow velocity essentially reached its asymptotic value within the Comptonization region. To check the self-consistency of this assumption, we compute the value of $u(r_\beta)$ for each set of model parameters considered, finding in most cases that $u(r_\beta) \gtrsim 0.75\, u_\infty$.

For the scattering dominated winds treated here and in Paper I, the radiation field can be far from Planckian; a reasonable conjecture is that the electron temperature tracks the inverse Compton temperature of the photons,

$$T_{IC} \equiv \frac{h}{4k}\frac{\int_0^\infty \nu^4 \bar{n} d\nu}{\int_0^\infty \nu^3 \bar{n} d\nu} \tag{3.6}$$

(defined here without regard to stimulated processes), since thermalization of the photons occurs via Compton scattering at such high radiation intensities. If the scattering were purely

elastic (Thomson scattering), then the inverse Compton temperature would decrease adiabatically as $n_e^{\gamma-1} = n_e^{1/3}$; the effect of *inelastic* scattering on the electron (i.e., inverse Compton) temperature is expressed by the "temperature function"

$$f(y) \equiv \frac{T_e}{T_{ei}} \left(\frac{n_e}{n_{ei}}\right)^{-1/3} \tag{3.7}$$

[where $f(0) = 1$], which when used along with equation (2.1) to eliminate T_e and n_e in equation (3.5) yields

$$\int_0^{y(r)} \frac{dt}{f(t)} = \Lambda \int_1^{r/r_i} \left(\frac{\tilde{u}}{\tilde{u}_i}\right)^{-7/3} \left(\frac{r}{r_i}\right)^{-8/3} d\left(\frac{r}{r_i}\right), \tag{3.8}$$

where the constant Λ is defined as

$$\Lambda \equiv \frac{r_i n_{ei} \sigma_T}{\tilde{u}_i} \frac{kT_{ei}}{m_e c^2} = \frac{1}{2x_i \tilde{u}_i^2} \frac{\dot{M}}{\dot{M}_E} \frac{kT_{ei}}{m_e c^2} . \tag{3.9}$$

The asymptotic value of the y-parameter (β) scales as the square root of Λ (Paper I, eq. [6.5]) for bremsstrahlung, making Λ the injection radius parameter which most sensitively differentiates between the radiative properties of different astrophysical systems.

IV. OBSERVABLE PROPERTIES

To calculate the physical properties of a model wind, one begins by choosing values for T_i, the central mass M, the dimensionless energy generation radius x_0, and either $\dot{M}/\dot{M}_E$ or L/L_E (determined from observations of the object under consideration). Using T_i and x_0, equations (3.3) and (3.4) set the dimensionless injection radius x_i, from which one can calculate $\tilde{u}_i$ and x_c by solving equations (2.2), (2.8), (2.9), and (2.13). With x_c fixed, equations (2.2), (2.8), and (2.13) yield $\tilde{u}(x)$ (which is in general a double-valued function because of the quadratic term in eq. [2.2]; one branch corresponds to inflow and the other to outflow), and using the chosen value for $\dot{M}/\dot{M}_E$ (or L/L_E), equation (2.23) determines L/L_E (or $\dot{M}/\dot{M}_E$), so that either way one may compute ρ_i and n_{ei} using equation (2.1). With our knowledge of $\dot{M}$, $\tilde{u}_i$, and the photon energy density at the injection radius $U_{ri} = 3\rho_i T_i c^2$, we can calculate the heating rate per unit area [accurate to $O(u_i)$] by summing the kinetic and advected fluxes at the injection radius,

$$F_i = \tfrac{4}{3} U_{ri} u_i c + \tfrac{1}{2} \rho_i u_i^3 c^3 , \tag{4.1}$$

where u_i is given by equation (2.7).

To determine the radiative properties of our model wind, we first need to set T_{ei} in equation (3.9) for Λ. It is convenient to consider an optically thin bremsstrahlung injection spectrum, since this case is treated in detail in Paper I (see eq. [4.3] and § VI). The emissivity (averaged over the injection region) ϵ_i is given in the case of bremsstrahlung by $\epsilon_i = \epsilon_{ff} \approx (1.4 \times 10^{-27}) n_{e0}^2 T_{ei}^{1/2} (1 + 4.4 \times 10^{-10} T_{ei})$ in cgs units, where n_{e0} is the mean electron number density in the injection region (generally $\sim$few times n_{ei}). The net heating rate per unit area is given in terms of the emissivity by $(1 - x_0^{-1})^{-1/2} H r_S \epsilon_i$ (where the factor in parenthesis adjusts the radiation pressure scale height to the local frame), which in a steady state must equal F_i given by equation (4.1), allowing us to estimate T_{ei}. We next need to specify the form of the temperature function $f(y)$ (eq. [3.7]). In Paper I, we show that within what we term the "equilibration region" ($r_i < r \leq r_{eq}$, the region within which T_e rapidly equilibrates to T_{IC}), $f(y)$ obeys

$$e^{4(R-\kappa)y} = \left(\frac{R-f}{R-1}\right)^R \left(\frac{\kappa-1}{\kappa-f}\right)^\kappa , \tag{4.2}$$

and that for $r_{eq} \leq r < r_\beta$, $f(y)$ varies as

$$f(y) = \frac{B}{1 + Cy} , \tag{4.3}$$

where the constants B and C are set by R using equation (6.6) of Paper I, $\kappa \equiv T_{ICi}/T_{ei}$, and

$$R \equiv 2 \frac{P_{ri}}{P_{gi}} + 1 = \frac{m_H c^2}{kT_{ei}} T_i + 1 . \tag{4.4}$$

Using equations (4.2) and (4.3), the integral on the left side of equation (3.8) can be expressed as

$$\int_0^y \frac{dt}{f(t)} = \frac{1}{4(R-\kappa)} \ln\left[\left(\frac{R-f_{eq}}{R-1}\right)\left(\frac{\kappa-1}{\kappa-f_{eq}}\right)\right] + \frac{1}{B}\left[y - y_{eq} + \frac{C}{2}(y^2 - y_{eq}^2)\right] \tag{4.5}$$

for $y > y_{eq}$, where $y_{eq} \equiv y(r_{eq})$ and $f_{eq} \equiv f(y_{eq})$. By numerically carrying out the integration on the right side of equation (3.8), we can solve for $y(r)$ and β. In Figure 3 we display y as a function of r for various values of x_0, T_i, T_{ei}, and $\dot{M}/\dot{M}_E$. The specific luminosity measured by a stationary observer at infinity is given by

$$L_\nu(\nu) = \frac{32h\pi^2 r_p^2}{c^2} \left(\frac{1-u_\infty}{1+u_\infty}\right) \nu^3 \bar{n}\left[\tilde{\chi}\left(\frac{1-u_\infty}{1+u_\infty}\right)^{1/2}, r_p\right], \tag{4.6}$$

where $\tilde{\chi} \equiv h\nu/kT_e(r_\beta)$ and the occupation number $\bar{n}$ is calculated using equation (5.4) of Paper I. In Figure 4 we show plots of the specific luminosity for parameters typical of X-ray bursters (Fig. 4*a*) and AGNs (Fig. 4*b*), when the initial spectrum corresponds to optically thin bremsstrahlung. For comparison, we have included Planck functions

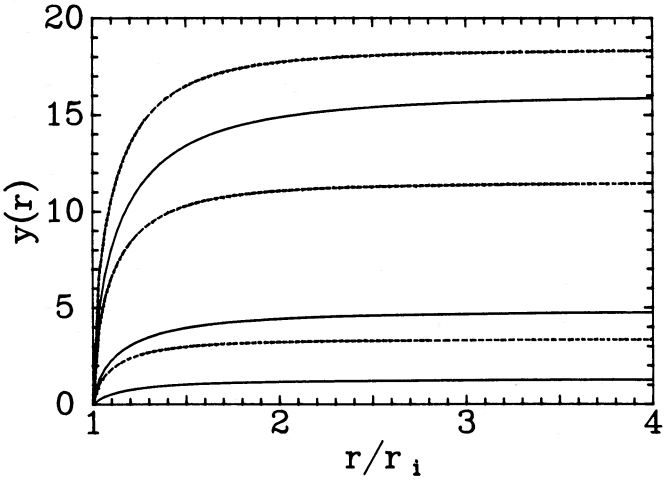

FIG. 3.—Variation of the Compton y-parameter (eq. [3.5]) is plotted as a function of r/r_i. Solid curves were calculated using the X-ray burster parameters listed in note (a) of Table 1, with the upper, middle, and lower curves corresponding to $\dot{M}/\dot{M}_E = 10^4$, 10^3, and 10^2, respectively. Dashed curves were calculated using the AGN parameters listed in note (b) of Table 1, with the upper, middle, and lower curves corresponding to $\dot{M}/\dot{M}_E = 2.5 \times 10^3$, 10^3, and 10^2, respectively.

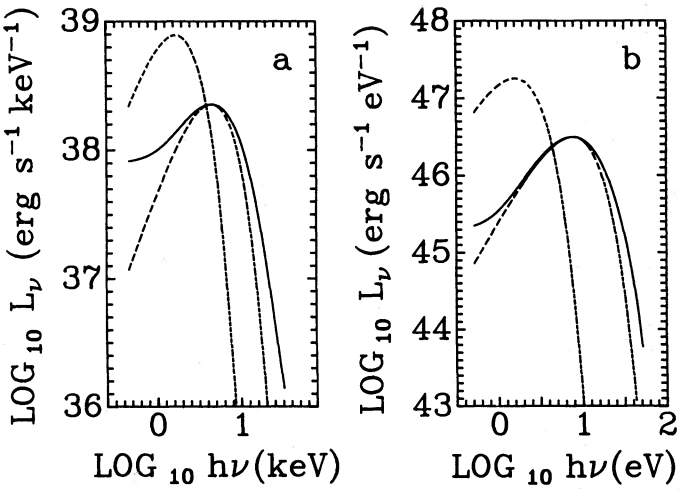

FIG. 4.—Specific luminosity measured by a stationary observer at infinity (eq. [4.6]) is plotted for a bremsstrahlung injection spectrum with $r_\beta/\tilde{r}_t = 0.1$ using (*a*) the X-ray burster parameters listed in note (a) of Table 1, along with $\dot{M}/\dot{M}_E = 130$; (*b*) the AGN parameters listed in note (b) of Table 1, along with $\dot{M}/\dot{M}_E = 800$. For comparison, we have included Planck functions (*dashed lines*) evaluated at the color and effective temperatures of the calculated spectra. For the plots in (*a*), $l_{obs} = 12.1$, $T_{color} = 1.8 \times 10^7$ K, $T_{eff} = 7.0 \times 10^6$ K, and $r_p = 86.3\, r_S$. For the plots in (*b*), $l_{obs} = 3.7$, $T_{color} = 3.2 \times 10^4$ K, $T_{eff} = 6.5 \times 10^3$ K, and $r_p = 2022\, r_S$. The spectral hardening that is characteristic of static scattering atmospheres is also apparent in these dynamical cases; unlike the static scenarios, the emergent luminosities far exceed L_E.

with temperatures equal to the observed color temperature and the effective temperature at the photosphere.

The color temperature of the spectrum apparent to an observer comoving with the flow is equal to $\tilde{\chi}_p\, T_e(r_\beta)/2.82$, where $\tilde{\chi} = \tilde{\chi}_p$ at the peak of the observed energy spectrum. To calculate the color temperature measured by a distant observer who is *stationary* with respect to the central object, we use

$$T_{color} = 0.355 \tilde{\chi}_p\, T_e(r_\beta) \left(\frac{1+u_\infty}{1-u_\infty}\right)^{1/2}, \qquad (4.7)$$

where the factor $[(1+u_\infty)/(1-u_\infty)]^{1/2}$ accounts for the Doppler shift between the moving and stationary frames. Using equation (3.7), the color temperature can be written in terms of T_{ei} as

$$T_{color} = 0.355 \tilde{\chi}_p\, T_{ei}\, f(\beta) \left[\frac{n_e(r_\beta)}{n_{ei}}\right]^{1/3} \left(\frac{1+u_\infty}{1-u_\infty}\right)^{1/2}. \qquad (4.8)$$

In Figure 5 we plot the log of the color temperature as a function of log T_{ei} for various values of x_0, T_i, and $a \equiv (\dot{M}/\dot{M}_E)(T_{ei}/10^{11}\ \mathrm{K})$. To understand the power-law relationship evidenced by the straight lines, note that by choosing values for T_i, x_0, and $\dot{M}T_{ei}$, we have implicitly set x_i, $\tilde{u}_i$, x_c, and $\tilde{u}_\infty$. Taking r_β to be some fixed fraction of $\tilde{r}_t$, mass conservation (eq. [2.1]) then yields $n_e(r_\beta)/n_{ei} \propto \dot{M}^{-2} \tilde{u}(r_\beta)^{-1}$. Combining this with the conditions $\dot{M} \propto a T_{ei}^{-1}$ and $\tilde{u}(r_\beta) \approx \tilde{u}_\infty$, we obtain $n_e(r_\beta)/n_{ei} \propto T_{ei}^2$. Since $\tilde{\chi}_p$ and $f(y)$ are relatively insensitive functions of T_i and T_{ei}, and $f(\beta) \approx \beta^{-1} \approx \Lambda^{-1/2}$ for bremsstrahlung (Paper I, eq. [6.5]), equation (4.8) yields the proportionality

$$T_{color} \propto \Lambda^{-7/6} T_{ei}^{5/3}, \qquad (4.9)$$

which is borne out in Figure 5.

In concluding this section, we point out that if one knows the values of M, L_∞, x_0, $\dot{M}$, and T_{color} for a particular object, then all of the other parameters can be determined uniquely. Beginning with equation (2.23), one obtains x_c for given $\dot{M}$ and L_∞. Using the resulting run of $\tilde{u}(x)$ and equations (2.8), (2.13), (3.3), and (3.4), x_i and T_i can be computed for a given x_0. The next step is to pick an initial guess for T_{ei}, which in turn provides values for Λ (eq. [3.9]) and for R (eq. [4.4]). Equation (3.8) then yields β and r_β, which we can subsequently use in equation (4.8) to calculate T_{color}. By repeating the procedure until one has obtained the value of T_{ei} that leads to the correct T_{color}, all of the parameters can be set uniquely. In such a case, the presence of a dip in the photon ($\nu^2 \bar{n}$) spectrum would provide an independent value for β (Paper I, § V), and thus an autonomous check on the self-consistency of the theory.

Finally, in Table 1 we summarize the results obtained for the heating rate per unit area F_i (eq. [4.1]), the advected photon flux at the injection radius F_a (the second term in eq. [4.1]), the dimensionless heating rate $4\pi r_i^2 F_i/L_E$, the dimensionless luminosity observed at infinity $l_{obs} = (L_\infty/L_E)(1+u_\infty)/(1-u_\infty)$, the color temperature, and injection region emissivity ϵ_i and number density n_{ei}, the β (the asymptotic value of y), for various values of T_i, T_{ei}, x_0, $\dot{M}/\dot{M}_E$, and M. The heating rate is typically $\gg L_E$, since most of the radiative energy initially deposited in the wind is used up in accelerating the matter out of the potential well.

V. DISCUSSION AND SUMMARY

Here and in Paper I we have made various assumptions concerning the importance of the physical processes not treated in detail. We now reexamine the validity of each assumption, for an initial spectrum corresponding to optically thin bremsstrahlung emission.

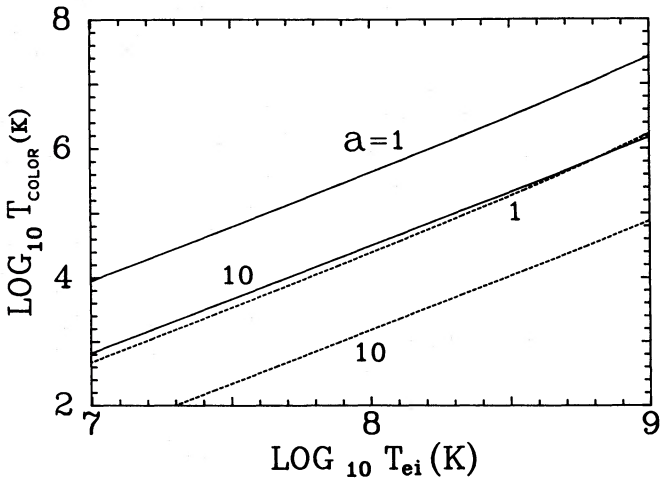

FIG. 5.—Color temperature measured by a stationary observer at infinity (eq. [4.8]) is plotted as a function of T_{ei} for a bremsstrahlung injection spectrum with $r_\beta/\tilde{r}_t = 0.1$ and the indicated value of $a \equiv (\dot{M}/\dot{M}_E)(T_{ei}/10^{11}\ \mathrm{K})$. Solid lines were calculated using the X-ray burster parameters $x_0 = 2.5$, $T_i = 0.1$, $x_c = 3.53$, $u_i = 0.28$, and $u_\infty = 0.57$, for which $\Lambda = 43a$. Dashed lines were calculated using the AGN parameters $x_0 = 3.0$, $T_i = 0.05$, $x_c = 20.44$, $u_i = 0.03$, and $u_\infty = 0.20$, for which $\Lambda = 3061a$. As discussed in the text, the straight lines reflect the proportionality $T_{color} \propto \Lambda^{-7/6} T_{ei}^{5/3}$.

TABLE 1

MODEL RESULTS FOR X-RAY BURSTERS AND AGNs

M ($M_\odot$)	F_i (ergs cm^{-2} s^{-1})	F_a (ergs cm^{-2} s^{-1})	$4\pi r_i^2 F_i/L_E$	l_{obs}	T_{color} (K)	ϵ_i (ergs cm^{-3} s^{-1})	n_{ei} (cm^{-3})	β	$\dot{M}/\dot{M}_E$
1.4 [a].....	3.9×10^{26}	3.6×10^{26}	50.8	11.1	2.6×10^{7}	9.8×10^{20}	7.0×10^{19}	1.26	10^2
	3.9×10^{27}	3.6×10^{27}	507.5	24.0	1.5×10^{6}	9.8×10^{21}	7.0×10^{20}	4.75	10^3
	3.9×10^{28}	3.6×10^{28}	5074.5	51.6	9.9×10^{4}	9.8×10^{22}	7.0×10^{21}	15.87	10^4
10^9 [b].....	2.1×10^{17}	2.1×10^{17}	23.6	1.8	5.2×10^{5}	9.6×10^{2}	7.1×10^{11}	3.35	10^2
	2.1×10^{18}	2.1×10^{18}	235.9	3.9	2.4×10^{4}	9.6×10^{3}	7.1×10^{12}	11.44	10^3
	2.1×10^{19}	2.1×10^{19}	2358.7	8.5	1.5×10^{3}	9.6×10^{4}	7.1×10^{13}	37.05	10^4

[a] For the X-ray burster ($M = 1.4\ M_\odot$) cases, we also have $r_\beta/\tilde{r}_t = 0.1$, $r_p/\tilde{r}_t = 2.0$, $x_0 = 2.5$, $T_i = 0.1$, $T_{ei} = 10^9$ K, $x_c = 3.53$, $x_i = 3.25$, $u_i = 0.28$, $u_\infty = 0.57$, and $U_{ri}/U_{ei} = 2179$.

[b] For the AGN ($M = 10^9\ M_\odot$) cases, we also have $r_\beta/\tilde{r}_t = 0.1$, $r_p/\tilde{r}_t = 5.3$, $x_0 = 3.0$, $T_i = 0.05$, $T_{ei} = 10^8$ K, $x_c = 20.44$, $x_i = 3.6$, $u_i = 0.03$, $u_\infty = 0.20$, and $U_{ri}/U_{ei} = 10894$.

a) *Bremsstrahlung Self-Absorption*

As discussed in § VI of Paper I, the bremsstrahlung self-absorption cutoff in the injection region, $\chi_0 = h\nu_0/kT_{ei}$, must satisfy

$$\chi_0 \ll 1 , \tag{5.1a}$$

where

$$\frac{\chi_0^3}{1 - e^{-\chi_0}} = (0.72\ \mathrm{K^3\ cm^3}) n_{ei}\, T_{ei}^{-3}\, \frac{P_{ri}}{P_{gi}} , \tag{5.1b}$$

in order to ensure that a large number of low-energy photons survive the injection region (i.e., in order to keep the spectrum optically thin), as we have assumed.

Likewise, the bremsstrahlung self-absorption cutoff due to thermalization within the Comptonization region, $\chi_c = h\nu_c/kT_e(r_\beta)$, must satisfy

$$\chi_c \ll 1 , \tag{5.2a}$$

where

$$N_{\mathrm{th}} = 1 = (4.1 \times 10^{-23}\ \mathrm{K^{7/2}\ cm^5}) \times \int_{r_i}^{r_\beta} n_e^2\, T_e^{-7/2} \left(\frac{h\nu_c}{kT_e}\right)^{-3} (1 - e^{-h\nu_c/kT_e})\, \frac{dr}{\tilde{u}} \tag{5.2b}$$

represents the average number of free-free thermalizations (absorptions) experienced by a photon of frequency ν_c between $r = r_i$ and $r = r_\beta$. Since we expect that $\chi_c \ll 1$, we can estimate χ_c by supposing that the density change across the Comptonization region is negligible, yielding

$$\chi_c < (6.0 \times 10^5\ \mathrm{K^{9/4}\ cm^{3/2}}) n_{ei}^{1/2}\, T_{ei}^{-9/4} f^{-9/4}(\beta) \beta^{1/2} . \tag{5.2c}$$

b) *Stimulated Compton Scattering*

Our neglect of stimulated Compton scattering is justified if the cutoff for the process, $\chi_s = h\nu_s/kT_{ei}$, satisfies

$$\chi_s \ll 1 , \tag{5.3a}$$

where

$$\bar{n}(\nu_s, r_i) = 1 = \frac{\chi_0^3}{1 - e^{-\chi_0}}\, e^{-\chi_s} \chi_s^{-3} \tag{5.3b}$$

is the phase space density of photons at the injection radius. The effect of stimulated Compton scattering must be taken into account when the occupation number exceeds unity.

c) *Double Compton Absorption*

The cutoff for the importance of double Compton absorption in the injection region,

$$\chi_{\mathrm{DC}} = \frac{h\nu_{\mathrm{DC}}}{kT_{ei}} = \left[\frac{\alpha n_r}{4\pi^2} \left(\frac{hc}{kT_{ei}}\right)^3 \frac{kT_{ei}}{m_e c^2}\right]^{1/2} , \tag{5.4a}$$

must satisfy

$$\chi_{\mathrm{DC}} \ll 1 \tag{5.4b}$$

(Lightman 1981; n_r is the photon number density and α is the fine-structure constant) in order to justify our neglect of the process, which becomes increasingly important in highly radiation dominated cases.

d) *Validity of the Assumptions*

All of the critical quantities listed above have been calculated along with the other model results and found to satisfy their respective criteria for the parameter domains discussed here. A more serious restriction on the theory is that imposed by our neglect of Klein-Nishina and pair production effects in the injection region, where the temperature may reach $\sim 17\%$ of $m_e c^2$ if our model is applied to X-ray burst sources, and considerably higher values if it is applied to gamma-ray transients; for AGNs the high-temperature effects are probably unimportant.

e) *Conclusion*

In the two papers composing this series, we have developed a theory which self-consistently describes both the radiative and the dynamical properties of supercritical winds. Such winds may play an important role in mass-losing quasars and AGNs, and could also be significant in the context of X-ray transients. By focusing our attention on supercritical cases, we are able (in Paper I) to simplify our treatment of the radiative transfer by dividing the wind into regions within which no more than two of the relevant physical processes (Compton scattering, adiabatic cooling, and diffusion) are important at once.

In this paper, we have examined the dynamics of supercritical winds and linked our results with those of Paper I to calculate the observable properties of such winds. The main results are contained in Figures 1, 4, and 5, and Table 1. In Figure 1 we see that luminosities far in excess of L_E can obtain if the supercritical outflow passes through a sonic point located deep within the relativistic potential. Such super-Eddington

luminosities are possible because the sonic radius of the flow is well within the trapping radius. In Figure 4 we compare our results for the specific luminosity with Planck functions at the color and effective temperatures, and in Figure 5 we depict the color temperature observed at infinity (for a bremsstrahlung initial spectrum) as a function of T_{ei} and other model parameters. Color temperatures high enough ($\sim 3 \times 10^7$ K) to accommodate observations of X-ray bursts (Lewin and Joss 1981) and low enough ($\lesssim 3 \times 10^4$ K) to explain the ultraviolet and soft X-ray features associated with AGNs (Blandford 1984; Arnaud *et al.* 1985) can be produced by the scenario presented here.

It has been pointed out to us that our treatment of the problem makes no reference to the type of outer boundary condition (relating the emerging flux of radiation to conditions at some reference optical depth) which comes into play in *static* electron scattering atmospheres. When the scattering gas is in hydrostatic equilibrium, diffusion dominates the radiation transport throughout the entire atmosphere, and the outer boundary condition determines the rate of escape of the photons (Ivanov 1973). The difference here is that the atmosphere is moving, and consequently it is *dynamical* effects which determine the photon escape rate. The conclusions presented in this paper are valid provided the throttle in the flow (at $r = r_c$) is well within the trapping radius, so that most of the momentum transfer occurs before diffusion becomes important.

In the case of X-ray bursts, the heating rates typically called for by the theory are far beyond the capabilities of an energy generation mechanism proposed so far. We direct the theory more toward quasars and AGNs because the energy generation rates are potentially much higher for black holes than for neutron stars (which seem to be associated with X-ray transients), and because all of the densities in the theory scale as M^{-1} (which makes most of our assumptions more plausible at higher values of M). Although we have not included all of the physics which one might deem appropriate in treating the problem, we nevertheless feel that such supercritical wind models provide an interesting alternative to the status quo interpretation of ultraviolet and moderate energy X-ray continuum features.

This research was supported by National Science Foundation grant AST83-51997, by NASA Astrophysical Theory Center grant NAGW-766, and by grants from Ball Aerospace Systems Division, Rockwell International Corporation, and the Exxon Education Foundation.

REFERENCES

Abramowitz, M., and Stegun, I. A. 1970, *Handbook of Mathematical Functions* (New York: Dover).
Arnaud, K. A., *et al.* 1985, *M.N.R.A.S.*, **217**, 105.
Becker, P. A., and Begelman, M. C. 1986, *Ap. J.*, **310**, 534 (Paper I).
Begelman, M. C. 1978, *Astr. Ap.*, **70**, 583.
Begelman, M. C., and Rees, M. J. 1983, in *Astrophysical Jets*, ed. A. Ferrari and A. G. Pacholczyk (Dordrecht: Reidel), p. 215.
———. 1984, *M.N.R.A.S.*, **206**, 209.
Blandford, R. D. 1984, preprint.
Canizares, C. R., and Kruper, J. 1984, *Ap. J. (Letters)*, **278**, L99.
Castor, J. I., Lutz, J. H., and Seaton, M. J. 1981, *M.N.R.A.S.*, **194**, 547.
Drew, J. E., and Boksenberg, A. 1984, *M.N.R.A.S.*, **211**, 813.
Ebisuzaki, T., Hanawa, T., and Sugimoto, D. 1984, *Pub. Astr. Soc. Japan*, **36**, 551.
Ebisuzaki, T., and Nomoto, K. 1985, in *Galactic and Extragalactic X-Ray Sources*, ed. Y. Tanaka and W. H. G. Lewin (Tokyo: Institute of Space and Astronautical Science), p. 101.
Hanawa, T., and Sugimoto, D. 1982, *Pub. Astr. Soc. Japan*, **34**, 1.
Inoue, H., Waki, I., Koyama, K., Matsuoka, M., Ohashi, T., Tanaka, Y., and Tsunemi, H. 1984, *Pub. Astr. Soc. Japan*, **36**, 831.
Ivanov, V. 1973, *Transfer of Radiation in Spectral Lines* (Washington, DC: NBS).
Krolik, J. H., Kallman, T. R., Fabian, A. C., and Rees, M. J. 1985, *Ap. J.*, **295**, 104.
Lewin, W. H. G., and Joss, P. C. 1981, *Space Sci. Rev.*, **28**, 3.
Lightman, A. P. 1981, *Ap. J.*, **244**, 392.
London, R. A., Taam, R. E., and Howard, W. M. 1984, *Ap. J. (Letters)*, **287**, L27.
———. 1986, *Ap. J.*, **306**, 170.
Marshall, H. L. 1982, *Ap. J.*, **260**, 815.
McCray, R. 1981, *Ann. NY Acad.* Sci., **375**, 391.
Meier, D. L. 1979, *Ap. J.*, **233**, 664.
———. 1982*a*, *Ap. J.*, **256**, 681.
———. 1982*b*, *Ap. J.*, **256**, 693.
———. 1982*c*, *Ap. J.*, **256**, 706.
Michel, F. C. 1972, *Ap. Space Sci.*, **15**, 153.
Paczyński, B. 1983, *Ap. J.*, **267**, 315.
Perry, J. J., and Dyson, J. E. 1985, *M.N.R.A.S.*, **213**, 665.
Swank, J. H., Taam, R. E., and White, N. E. 1984, *Ap. J.*, **277**, 274.
Taam, R. E. 1982, *Ap. J.*, **258**, 761.
Turnshek, D. A. 1984, *Ap. J.*, **280**, 51.
Wallace, R. K., Woosley, S. E., and Weaver, T. A. 1982, *Ap. J.*, **258**, 696.
Weinberg, S. 1972, *Gravitation and Cosmology* (New York: Wiley).
Weymann, R. J., Carswell, R. F., and Smith, M. G. 1981, *Ann. Rev. Astr. Ap.*, **19**, 41.

PETER A. BECKER and MITCHELL C. BEGELMAN: Joint Institute for Laboratory Astrophysics, University of Colorado, Boulder, CO 80309-0440